Supporting Information

Atomic scale control of spin current transmission at interfaces

Mohamed Amine Wahada,[1,*] Ersoy Şaşıoğlu,[2] Wolfgang Hoppe,[3]
Xilin Zhou,[1] Hakan Deniz,[1] Reza Rouzegar,[4] Tobias Kampfrath,[4]
Ingrid Mertig,[2] Stuart S. P. Parkin,[1] and Georg Woltersdorf[3,†]

[1]*Max Planck Institute for Microstructure Physics, Weinberg 2 06120 Halle, Germany*

[2]*Institute of Physics, Martin Luther University Halle-Wittenberg, Von-Seckendorff-Platz 1, 06120 Halle, Germany*

[3]*Institute of Physics, Martin Luther University Halle-Wittenberg, von Danckelmann Platz 3, 06120 Halle, Germany*

[4]*Institute of Physics, Freie Universität Berlin, Arnimalee 14, 01120 Berlin, Germany*

[*] awahada@mpi-halle.mpg.de

[†] georg.woltersdorf@physik.uni-halle.de

S1. METHODS

Samples. For the experiments, two sets of FM/HM bilayers with ultrathin MgO interlayers are perepared. The layer stacks have the following structure TaN(1.5)/CoFeB(2)/MgO(t)/Pt(4)/TaN(1.5) and TaN(1.5)/CoFeB(2)/MgO(t)/Ta(3)/TaN(1.5) all grown on Sapphire(0001) substrate. All the thicknesses of the individual layers are in nanometers. The MgO thickness t has been varied between 0 and 1.7 nm. All layers have been grown by DC Magnetron sputtering at ultra high vacuum at a base pressure of 3 mTorr execpt for MgO grown by RF-sputtering using an off-axis gun tilted at a right angle from the substrate plane. The MgO layer grows crystalline on amorphous CoFeB as shown in Figure S5 using transmission electron microscopy (TEM) micrograph confirming the (001) orientation of MgO. To ensure the precision of the layer growth for all layers, all deposition rates were calibrated and monitored by a quartz crystal microbalance. Atomic force microscopy has been performed on all samples as shown in Figures S1 and S2. For both sample series we show the root mean square roughness (RMS) to be below 2Å. We would like to point out that the insertion of the MgO interlayer has almost no measurable impact on the conductivity of the layer stack (see Figure S2). In particular this implies that the Ta layer remains in the highly resistive β-phase for all MgO interlayers.

Ultrafast inverse SHE. Our samples are excited with an amplified Yb:KGW femtosecond laser system operating at 1030 nm wavelength with a 300 fs pulse width. On the samples the laser fluence is set to around 0.5 mJ/cm^2 unless otherwise indicated. For signal detection, an rf-probe tip connected to a sampling oscilloscope (synchronized with the laser) is used to measure the ISHE voltage signals. The bandwidth of the probe tip and the oscilloscope is limited to 50 GHz. Therefore the measured signal is a convolution of the ultrafast ISHE signal with the response function of the rf circuit [1]. An external magnetic field is set parallel to the sample plane and perpendicular to the ISHE voltage. The signal of interest is taken as the difference between the two voltages from the two opposite field orientations to eliminate other possible signal sources.

Ferromagnetic resonance (Spin pumping) Samples are placed on top of a broadband coplanar waveguide and can be excited with rf field frequencies between 2 and 20 GHz. The field swept linewidth for the ferromagnetic resonance is extracted by fitting the experimental data to Lorentzian line shapes. The observed slope of the linewidth determines the Gilbert

damping parameter. The enhancement of the Gilbert damping due to the presence of the HM layers is attributed to spin pumping and spin relaxation in the HM layer. For each sample, the Gilbert damping was averaged over three in plane directions (0, 45° and 90 ° angles) of the sample with respect to the external magnetic field.

Transport calculations To model our system, we use interface builder in the QuantumATK package to construct a common unit cell for Fe/MgO/HM trilayers. The MgO matches well the bcc Fe in its (001) orientation where the oxygen atoms face directly the Fe atoms. We consider HM=Pt and HM=Ta. For the case of Pt, we consider it in its body centered tetragonal structure giving a mismatch of 3% with bcc Fe. As for the case of Ta, We build a 1×3 supercell of Ta (110) in its body centered cubic phase. The MgO has been varied until 6MLs and to account for effective thicknesses less than one ML, we consider intermixing between the first Fe and HM ML at the interface and MgO. A sketch of the device structure with 4 ML of MgO and Ta as a HM is shown in supplementary Figure S6(a). Ground-state electronic structure calculations are carried out using DFT, implemented in the QuantumATK R-2020.09 package [2] with Perdew-Burke-Ernzerhof (PBE) parametrization of the generalized gradient approximation for the exchange-correlation (XC) functional [3]. We use PseudoDojo pseudopotentials [4] and LCAO basis sets. A dense $20 \times 20 \times 1$ ($20 \times 7 \times 1$) **k**-point grid for Pt case (Ta case) and a density mesh cutoff of 120 hartree are used. The total energy and forces converge to at least 1×10^{-4} eV and 0.01 eV/ Å, respectively. The transport calculations are carried out using DFT combined with the nonequilibrium Green's function method (NEGF). We use a $20 \times 20 \times 172$ ($20 \times 7 \times 172$) **k**-point grid for Pt and Ta case in self-consistent DFT-NEGF calculations. The current is calculated within a Landauer approach [57], where $I(V) = \frac{2e}{h} \sum_\sigma \int T^\sigma(E,V) \left[f_L(E,V) - f_R(E,V) \right] \mathrm{d}E$. Here V denotes the bias voltage, $T^\sigma(E,V)$ is the spin-dependent transmission coefficient for an electron with spin σ and $f_L(E,V)$ and $f_R(E,V)$ are the Fermi-Dirac distributions for the left and right leads which translates here to FM and HM, respectively. We assume that the electronic system is thermalized and thus temperature effects on transport properties can be taken into account via the Fermi-Dirac distribution function. The transmission coefficient $T^\sigma(E,V)$ is calculated using a 100×100 (100×34) **k**-point grid for the Pt and Ta cases.

S2. MAGNETIC MOMENT REDUCTION

In Figure S14, we present the non-magnetic DOS for the interface Fe (Co) atoms and compare them with the corresponding bulk DOS. In Stoner model of ferromagnetism, the condition $I \cdot N(E_F) \geq 1$ should be satisfied, where $N(E_F)$ is the non-magnetic DOS at the Fermi level and the Stoner parameter I can be related to the Hubbard U and Hund exchange J parameter as it has been discussed in Ref[5, 6]. We expect that the Stoner parameter I would not change substantially for the interface Fe (Co) atoms since the U and J parameters are less sensitive to the changes in local environment[7] and thus the behavior of the DOS at the Fermi level plays an essential role in suppression of the interface magnetic moments.

		Fe/Ta		**Fe/MgO/Ta**		**Fe/Pt**		**Fe/MgO/Pt**	
	Fe(B)	**Fe**	**Ta**	**Fe**	**Ta**	**Fe**	**Pt**	**Fe**	**Pt**
magnetic moment (μ_B)	2.3	0.80	-0.16	2.92	-0.002	2.92	0.2	2.89	-0.06
		0.57	-0.22	2.92	-0.03				
		1.13	-0.21	2.91	-0.03				

TABLE S1. Calculated magnetic moments for interfacial and bulk(B) layers in Fe/HM with and without one ML of MgO. For the case of Ta as a heavy metal, three atoms per layer are considered.

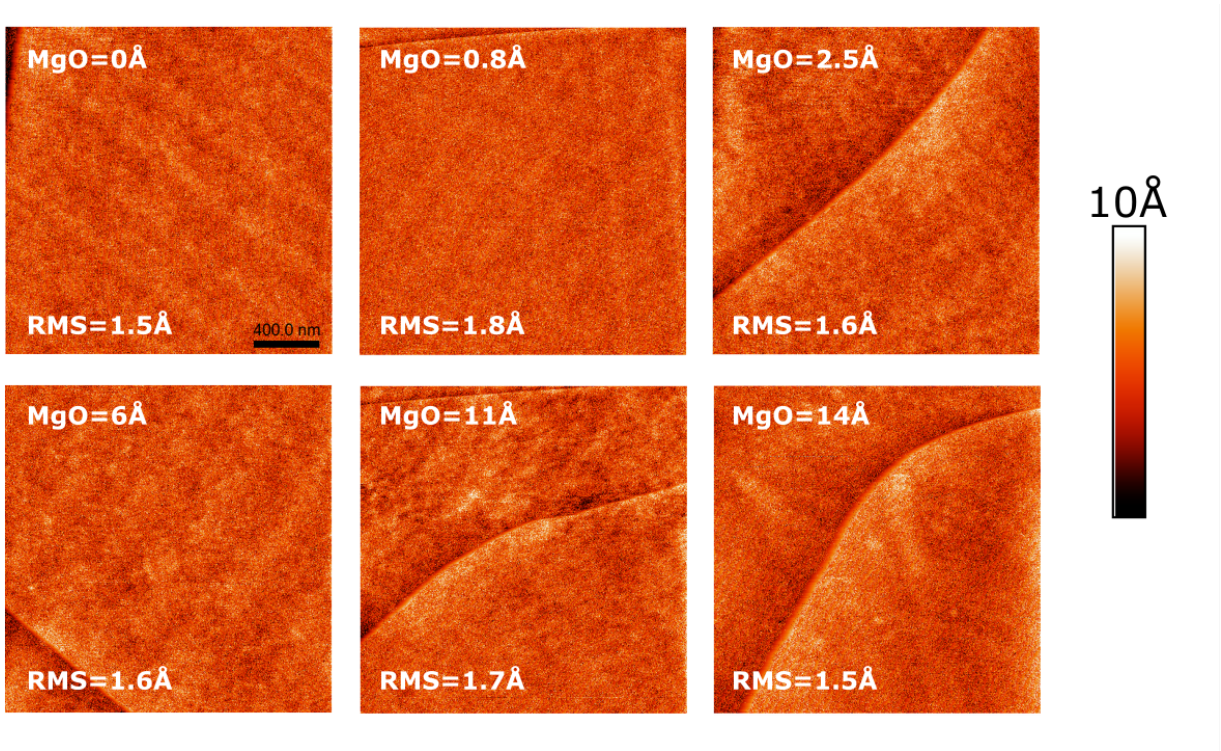

Figure S1. Atomic Force Microscopy scans of $2 \times 2\mu m^2$ areas the CoFeB/MgO/Pt samples for various MgO thicknesses. The root mean square roughness (RMS) is displayed for every micrograph.

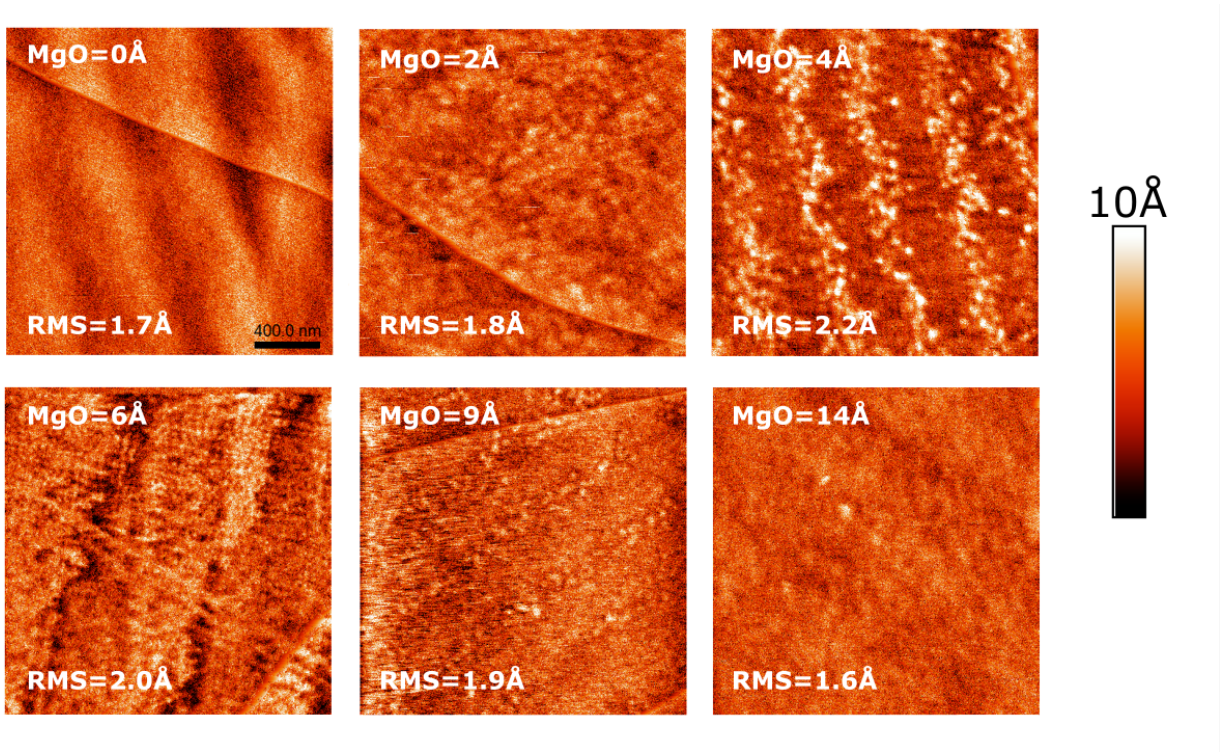

Figure S2. Atomic Force Microscopy scans of $2 \times 2\mu m^2$ areas the CoFeB/MgO/Ta samples for various MgO thicknesses. The root mean square roughness (RMS) is displayed for every micrograph.

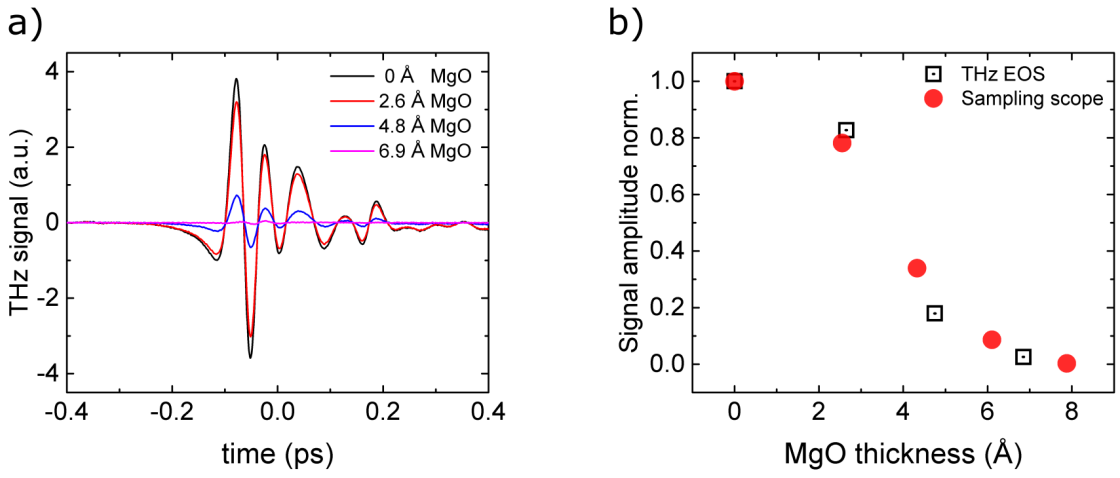

Figure S3. (a) Time resolved THz signals measured on CoFeB(2nm)/MgO/Pt(2nm) for different MgO thicknesses. (b) MgO thickness dependence of the root mean square value of the free space electro-optic sampling THz signals in comparison with the fast sampling scope technique used in our study for CoFeB/MgO/Pt.

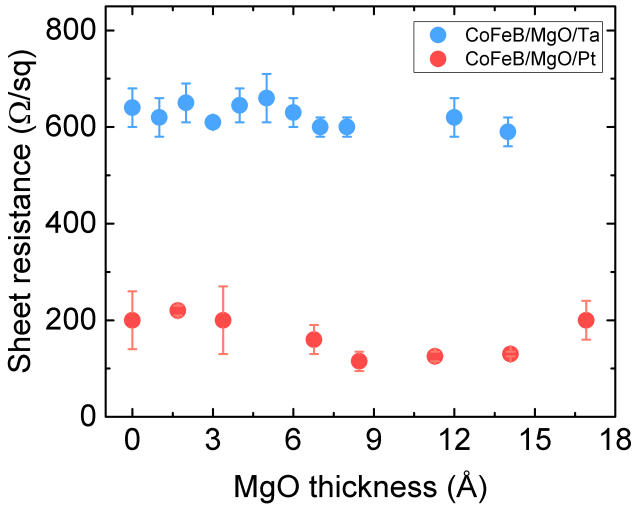

Figure S4. MgO thickness dependence of the sheet resistivity, measured with a 4 point probe method, for CoFeB/MgO/Ta and CoFeB/MgO/Pt.

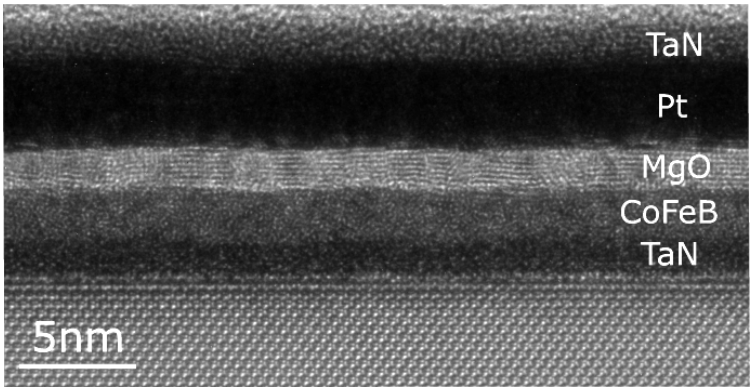

Figure S5. Transmission electron microscopy micrograph acquired at FEI TITAN 80-300 electron microscope showing the layered structure with Pt as a heavy metal and the MgO interlayer in its cubic phase with (001) orientation. From bottom to top: TaN(1.5), CoFeB(2), MgO(1.7), Pt(4), TaN(1.5). All thicknesses are in nm.

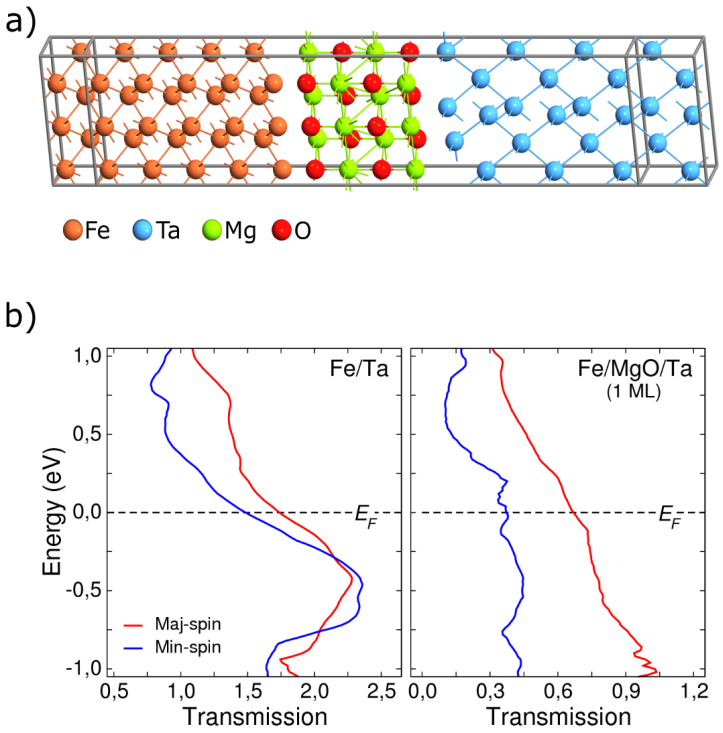

Figure S6. (a) The atomic structure of the Fe/MgO/Ta junction. (b) Spin-resolved transmission spectra for Fe/Ta and Fe/MgO/Ta junctions with one monolayer of MgO. Inset: voltage bias dependence of the ratio of the spin current transmission for Fe/MgO(1ML)/Ta compared to Fe/Ta

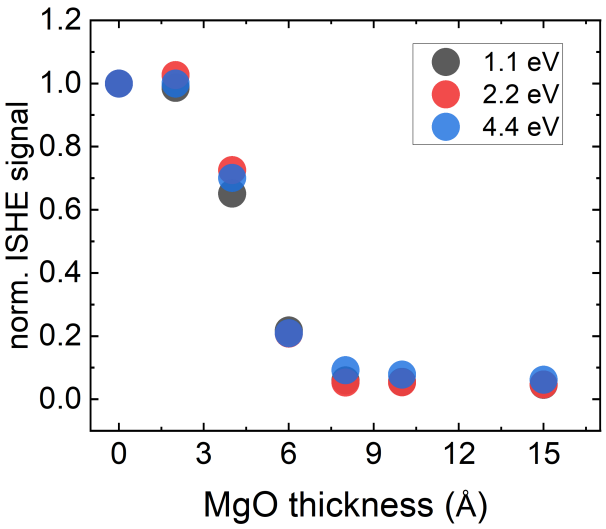

Figure S7. MgO thickness dependence of the normalized ISHE signal for various photon energies: 1.1eV, 2.2eV and 4.4eV.

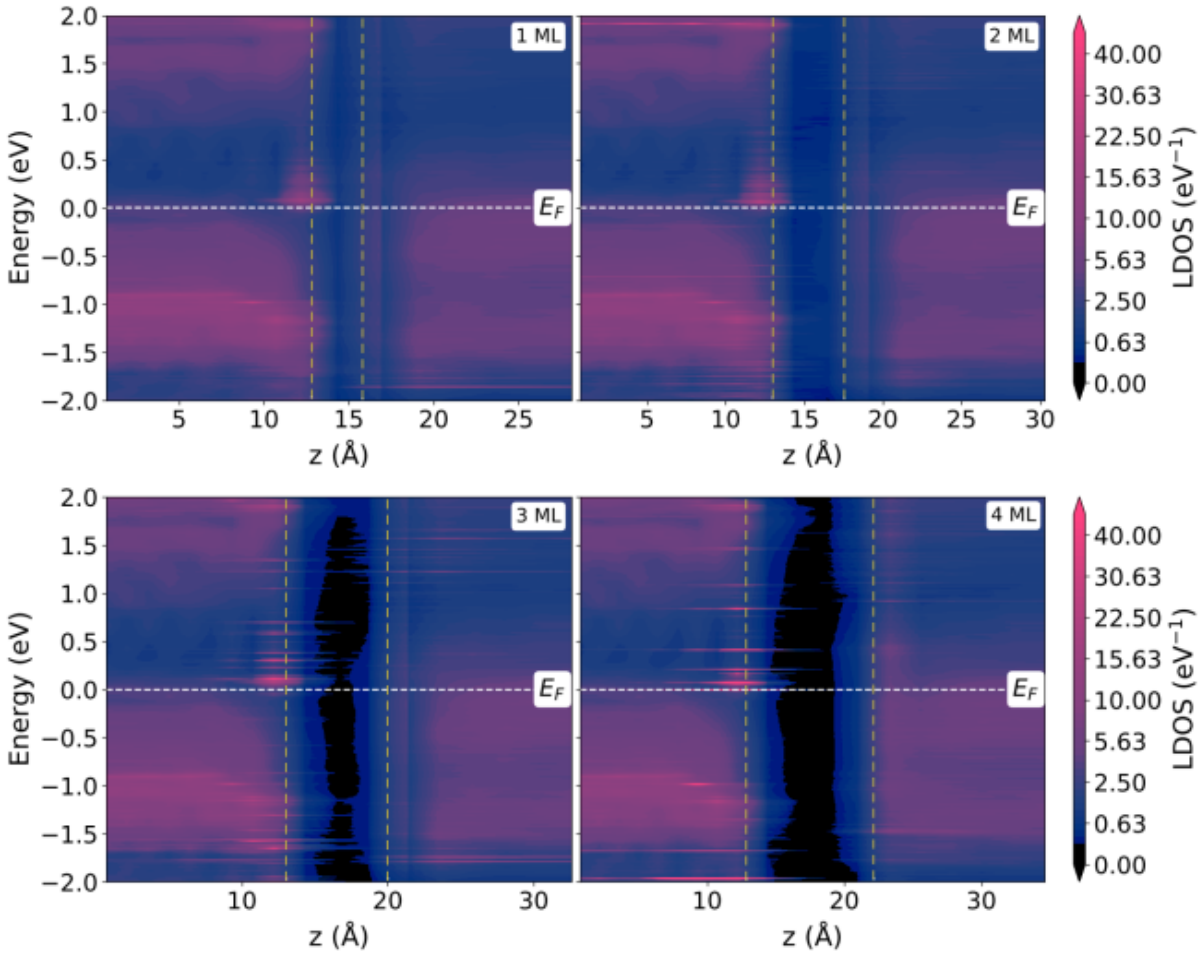

Figure S8. The zero-bias projected local density of states (LDOS) of the Fe/MgO/Ta junction for different monolayers of MgO barrier. The horizontal white dashed lines indicate the Fermi level. The vertical dashed lines denote the interface between Fe(left), MgO(middle) and Ta(right).

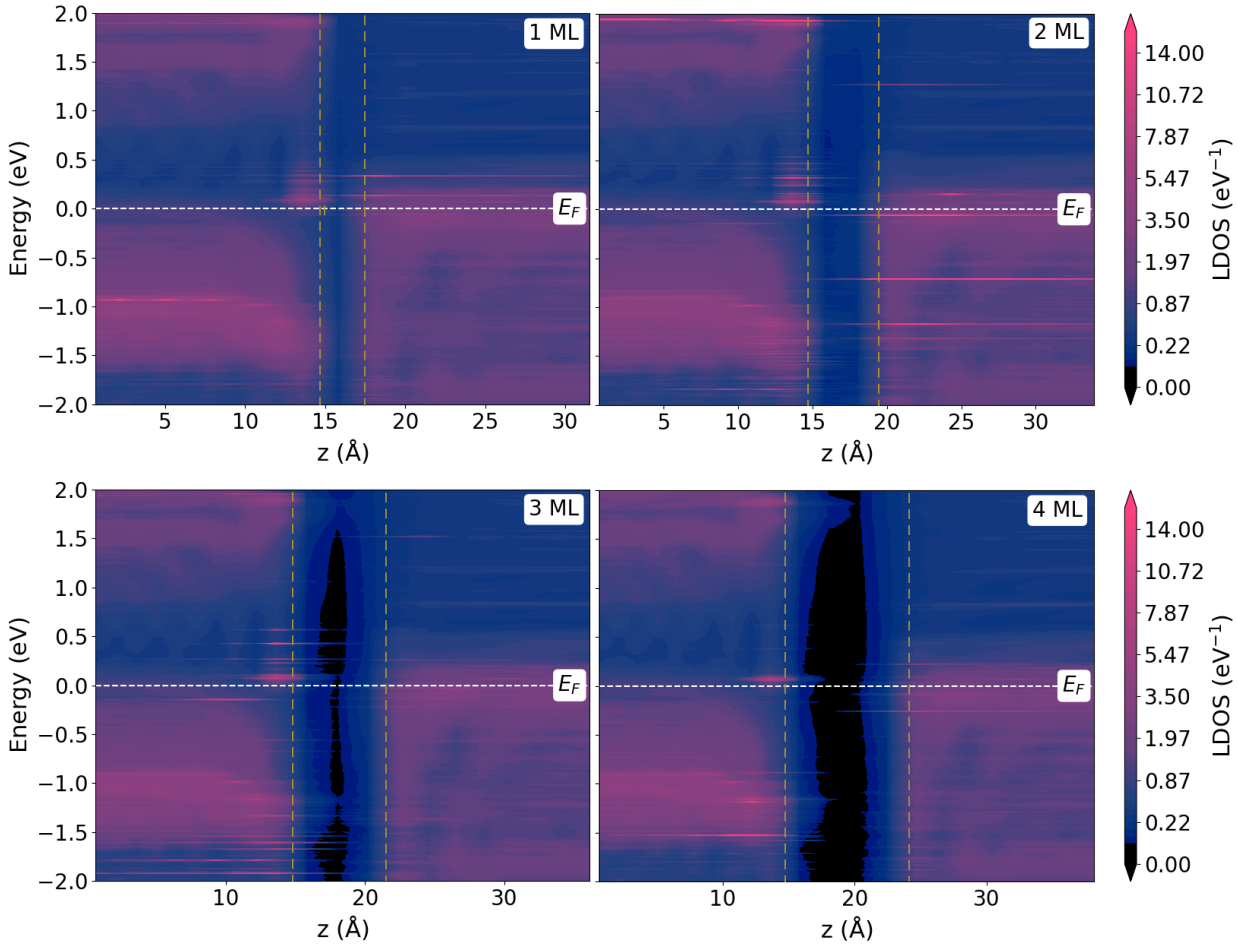

Figure S9. The zero-bias projected local density of states (LDOS) of the Fe/MgO/Pt junction for different monolayers of MgO barrier. The horizontal white dashed lines indicate the Fermi level. The vertical dashed lines denote the interface between Fe(left), MgO(middle) and Pt(right).

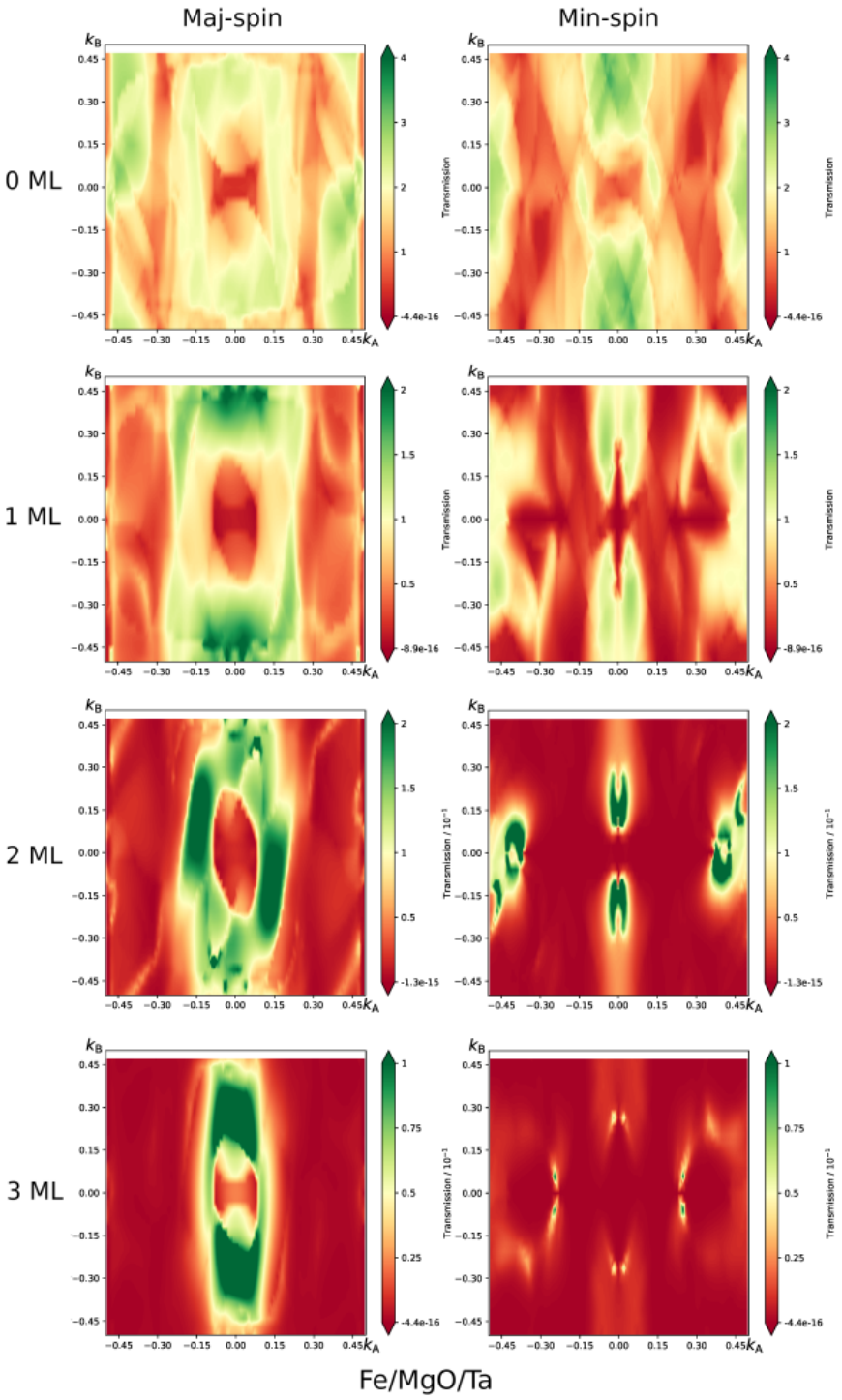

Figure S10. Spin resolved **k**-dependent transmission amplitudes of the spin current through the entire Fe/Ta structure for different monolayers of MgO interlayer.

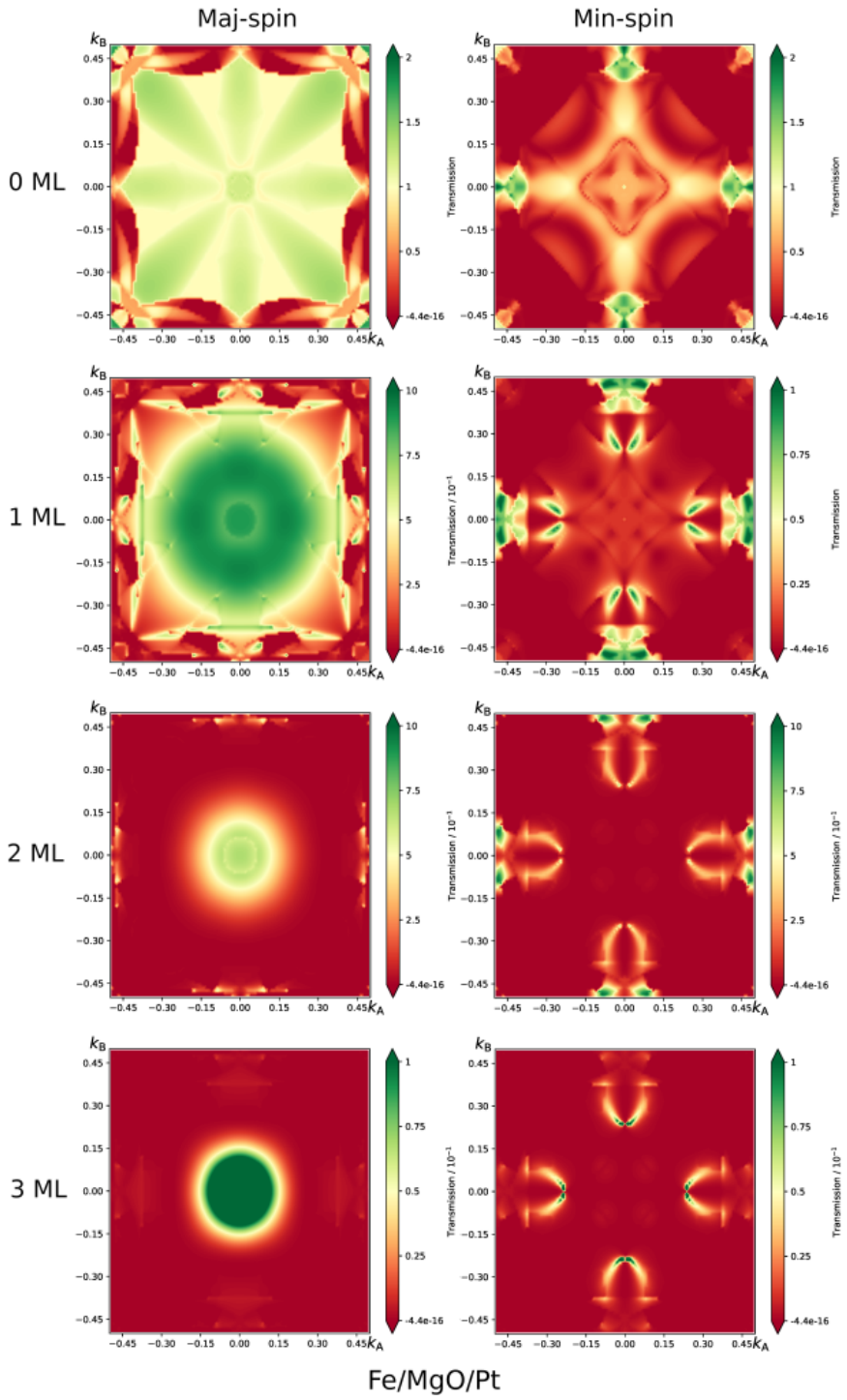

Figure S11. Spin resolved **k**-dependent transmission amplitudes of the spin current through the entire Fe/Pt structure for different monolayers of MgO interlayer.

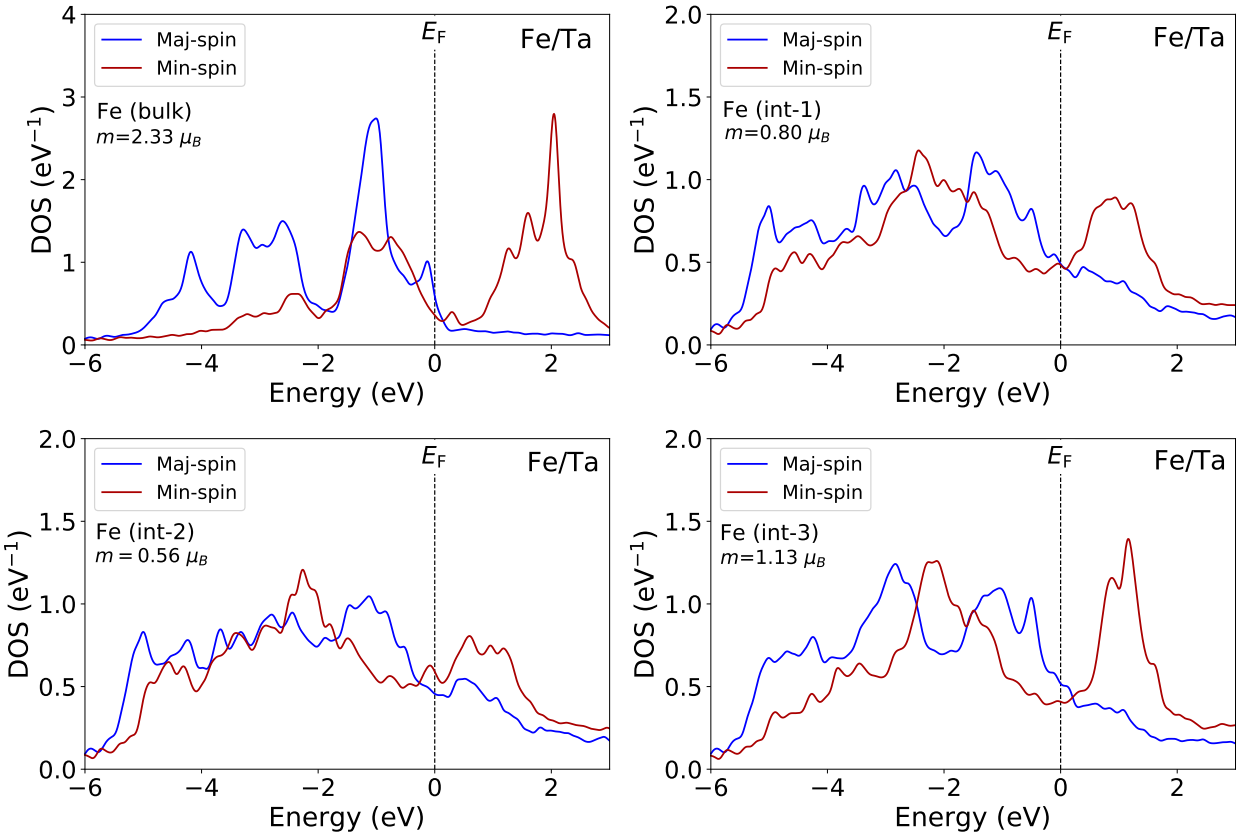

Figure S12. DOS for majority and minority spin for bulk Fe and the three different interfacial Fe at Fe/Ta interface. The magnetic moment is shown for all cases.

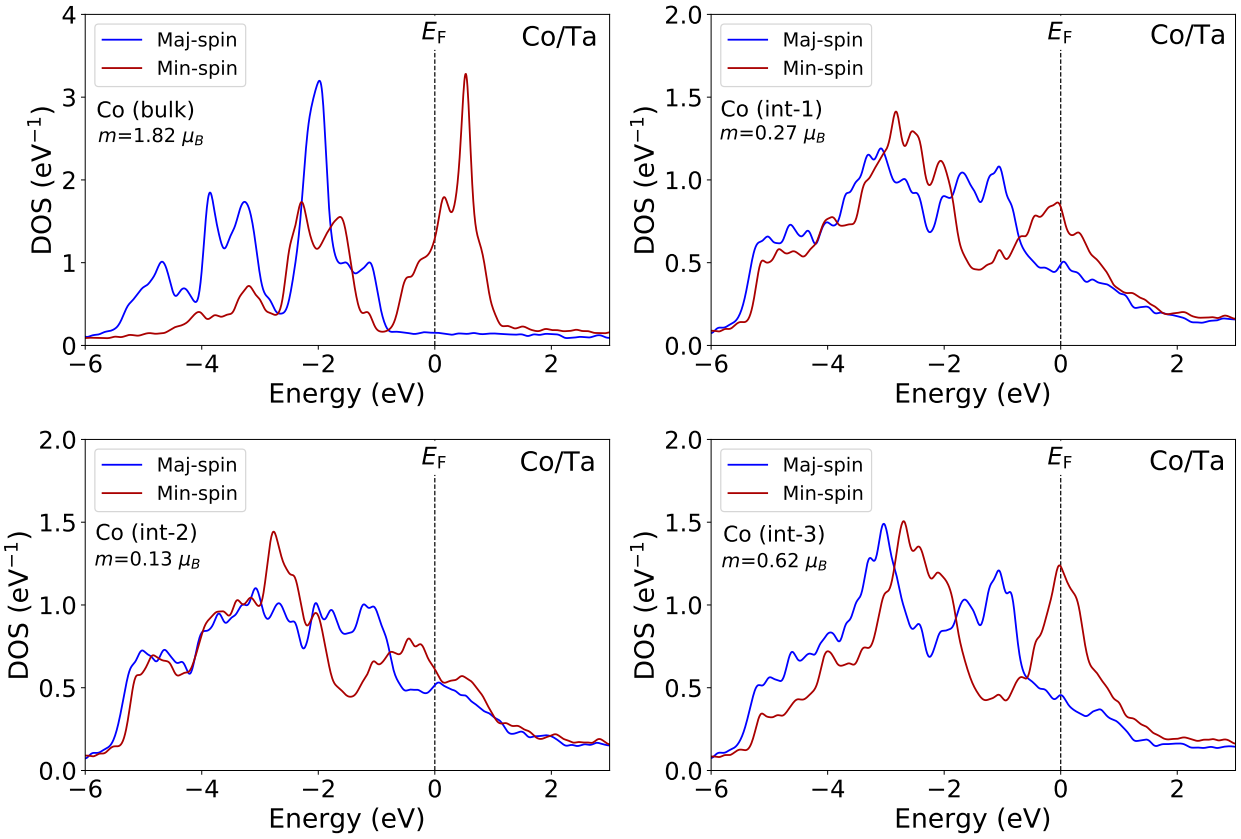

Figure S13. Density of states for majority and minority spin for bulk Co and the three different interfacial Co at Co/Ta interface. The magnetic moment is shown for all cases.

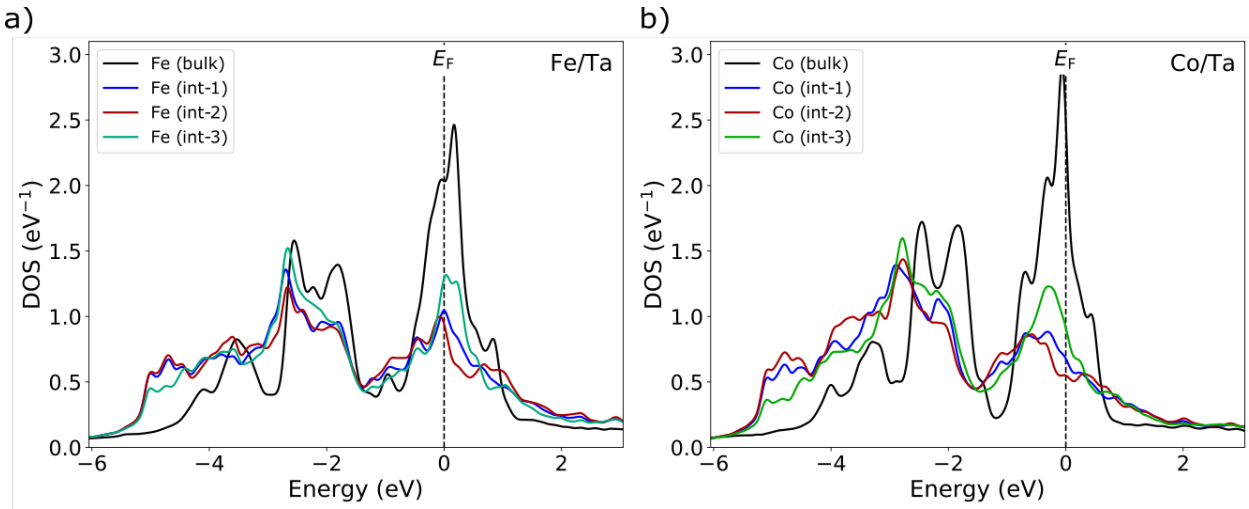

Figure S14. Non magnetic density of states for bulk Fe and the three interfacial Fe at Fe/Ta interface as well as for bulk Co and the three interfacial Co at Co/Ta interface.

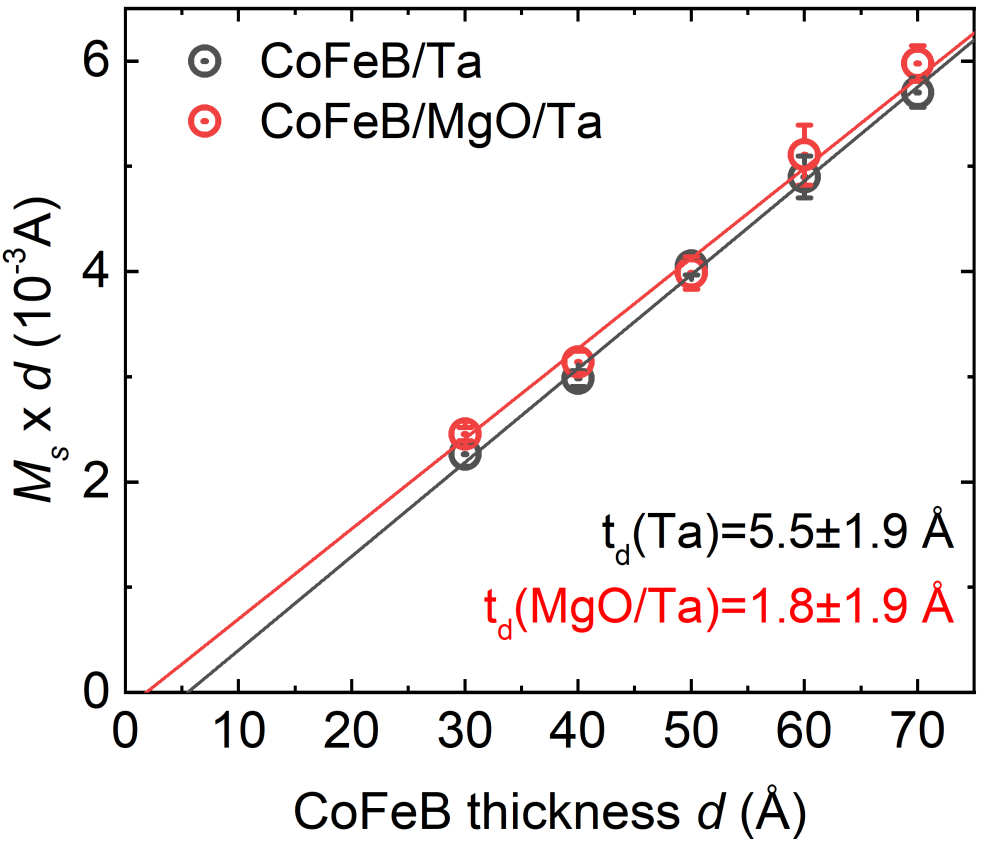

Figure S15. CoFeB thickness dependence of the saturation magnetization per area for CoFeB/20Ta and CoFeB/2MgO/20Ta. All thicknesses are in Å. The fit is a linear function used to extract the effective thickness of the non magnetic interface layer.

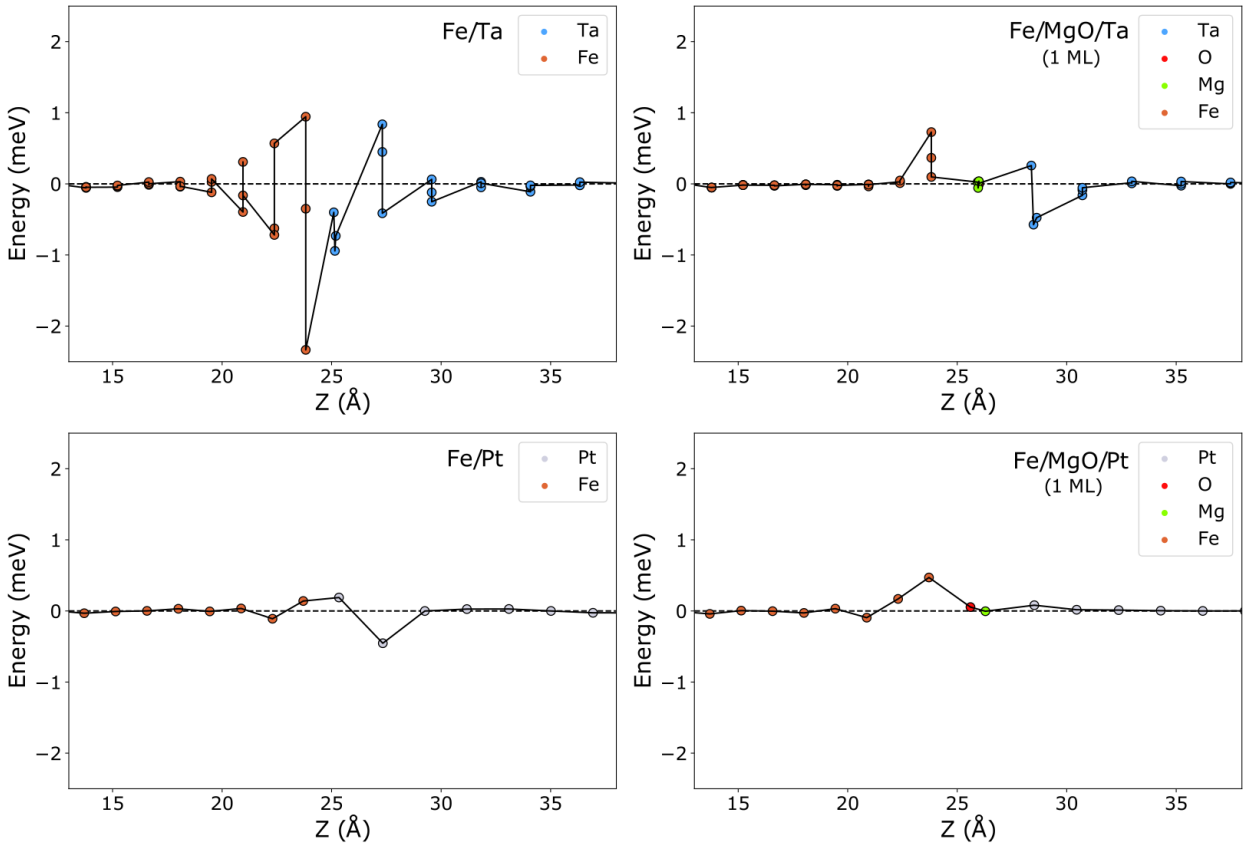

Figure S16. Local magnetic anisotropy energy for both heavy metals without MgO and with one ML of MgO.

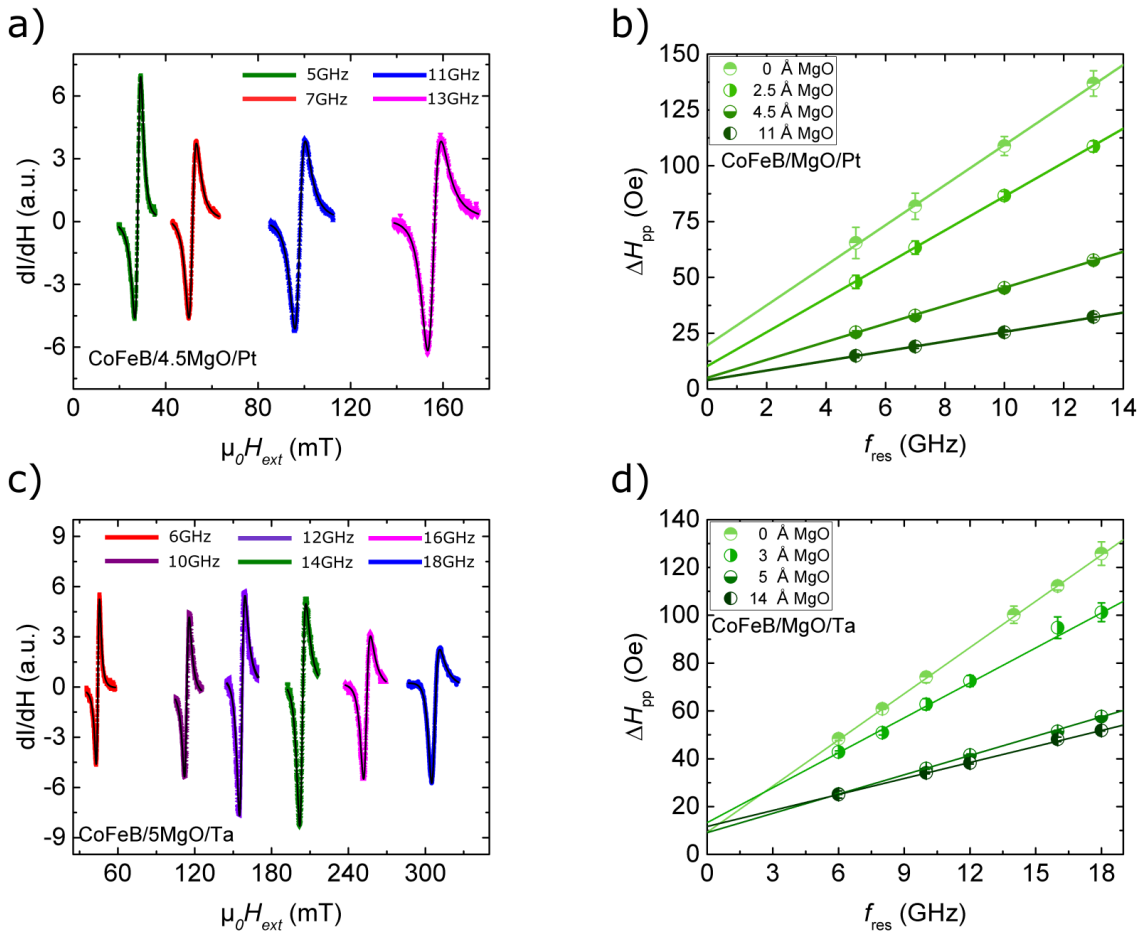

Figure S17. (a) and (c) Magnetic field dependence of the absorption spectra at the ferromagnetic resonance for various rf excitation frequencies for CoFeB/4.5MgO/Pt and CoFeB/5MgO/Ta respectively. (b) and (d) Frequency dependence of the ferromagnetic resonance linewidth for CoFeB/MgO/Pt and CoFeB/MgO/Ta respectively with various MgO thicknesses.

S3. REFERENCES

[1] Wolfgang Hoppe, Jonathan Weber, Saban Tirpanci, Oliver Gueckstock, Tobias Kampfrath, and Georg Woltersdorf, "On-chip generation of ultrafast current pulses by nanolayered spintronic terahertz emitters," ACS Applied Nano Materials **4**, 7454–7460 (2021).

[2] Søren Smidstrup, Daniele Stradi, Jess Wellendorff, Petr A Khomyakov, Ulrik G Vej-Hansen, Maeng-Eun Lee, Tushar Ghosh, Elvar Jónsson, Hannes Jónsson, and Kurt Stokbro, "First-principles Green's-function method for surface calculations: A pseudopotential localized basis set approach," *Phys. Rev. B* **96**, 195309 (2017).

[3] John P Perdew, Kieron Burke, and Matthias Ernzerhof, "Generalized gradient approximation made simple," *Phys. Rev. Lett.* **77**, 3865–3868 (1996).

[4] M. J. Van Setten, Matteo Giantomassi, Eric Bousquet, Matthieu J Verstraete, Don R Hamann, Xavier Gonze, and G-M Rignanese, "The PseudoDojo: Training and grading a 85 element optimized norm-conserving pseudopotential table," *Comput. Phys. Commun.* **226**, 39–54 (2018).

[5] Gernot Stollhoff, Andrzej M. Oleś, and Volker Heine, "Stoner exchange interaction in transition metals," *Phys. Rev. B* **41**, 7028 (1990).

[6] Ersoy Şaşıoğlu, Christoph Friedrich, and Stefan Blügel, "Effective coulomb interaction in transition metals from constrained random-phase approximation," *Phys. Rev. B* **83**, 121101 (2011).

[7] Ersoy Şaşıoğlu, Christoph Friedrich, and Stefan Blügel, "Strength of the effective coulomb interaction at metal and insulator surfaces," *Physical review letters* **109**, 146401 (2012).